Applied Numerical Modeling in Geomechanics – 2016 – Gómez, Detournay, Hart & Nelson (eds.) Paper: 10-01

Development of a proppant transport logic in *3DEC*

C. Detournay & J. Lemos
Itasca Consulting Group, Inc. Minneapolis, MN, USA

F. Zhang
Itasca Houston, Inc., IMaGE – Itasca Microseismic and Geomechanical Evaluation, Houston, TX, USA

ABSTRACT: Hydraulic fracturing is a technique, used in the oil and gas industry, to stimulate production. The fracturing treatment often involves the injection of proppant as a suspension in the fracturing fluid. After the end of injection, the fracture closes onto the proppant, and a conductive conduit is formed to allow the oil/gas to flow.

The transport and placement of proppant within the fracture is usually modeled by representing the proppant and fracturing fluid as a mixture, and this is the approach taken in the paper. It is assumed that the proppant particles are small compared to the fracture opening, and the quantity of proppant in the mixture is given by its volumetric concentration.

The logic takes into account fluid-mechanical coupling and several effects are represented, such as pack-formation (when the concentration reaches a given value, the proppant forms a pack, leaving only the fracturing fluid to flow through), bridging (when the proppant is no longer transported because the fracture width is small, compared to the particle size), proppant convection (when density gradients cause fluid motion in the fluid loaded with proppant), and settling (when the gravitational force on the proppant particles overcomes the viscous drag forces).

The paper describes the proppant logic and its numerical implementation in *3DEC*.Simple simulation examples are included to illustrate proppant transport in a fractured medium.

1 LOGIC OVERVIEW

The transport and placement of proppant within *3DEC* (Itasca 2013) joints is modeled by considering that, in the absence of gravity induced settling, the proppant and fluid move at the same velocity. The logic follows the general approach summarized by Adachi et al. (2007). It is assumed that the proppant particles are generally small compared to fracture width, and that the quantity of proppant in the fracture is given by its volumetric fraction. Also, the only mechanism to account for relative velocities between the proppant and the carrying fluid is gravity-induced settling.

When the proppant volumetric fraction reaches a saturation value, the slurry (mixture of fracturing fluid and proppant) behaves like a porous solid, and the proppant particles conform to a "pack". Also, if the joint aperture becomes small compared to particle diameter, the mobility of the proppant is inhibited, again forming a "pack" or "bridge". Thereafter, two effects are considered: first, the proppant pack is able to take the load from the closing fracture (mechanical effect), and second, only the carrying fluid is able to mobilize through the pores of the pack (fluid transport effect).

When settling is allowed to take place, the proppant velocity has an additional vector component, which acts in the direction of gravity, to account for particle settling. The settling rate is proportional to the Stoke's velocity (under gravity) of a particle of given size in a fluid of given

viscosity. Also, an empirical multiplication factor (a function of volumetric fraction) is applied to Stoke's velocity, to account for particle interaction and wall effects.

2 BASIC EQUATIONS

2.1 *Transport equations*

The advection (volume conservation) equation for the proppant volumetric fraction, c is

$$\frac{\partial(ca)}{\partial t} + \nabla.\left(ca\boldsymbol{v}_p\right) = 0 \tag{1}$$

where a is joint aperture, and $\boldsymbol{v}_p$ is the proppant velocity vector.

Coupling between Eq.(1) and the logic for fluid flow in *3DEC* is done via the slurry velocity, $\boldsymbol{v}$ which is obtained by solving the existing fluid flow equations, and noting that the relation between slurry flow rate, $\boldsymbol{q}$ (per unit width of the joint) and slurry velocity is:

$$\boldsymbol{v} = \frac{\boldsymbol{q}}{a} \tag{2}$$

When settling is allowed to take place, the proppant velocity is calculated from the slurry velocity using:

$$\boldsymbol{v}_p = \boldsymbol{v} + (1-c)\boldsymbol{v}_s \tag{3}$$

where $\boldsymbol{v}_s$ the slip velocity, is a vector parallel to the gravity acceleration $\boldsymbol{g}$. The magnitude of the slip velocity is calculated from Stokes equation, and a correction factor (function of the concentration) is applied to take into account the effect of proppant interaction and wall effects:

$$\boldsymbol{v}_s = f(c)\boldsymbol{v}_{stokes} \tag{4}$$

In Eq.(4), $\boldsymbol{v}_{stokes}$ is the Stokes drag law on a single particle:

$$\boldsymbol{v}_{Stokes} = \left(\rho_p - \rho_f\right)\frac{d_p^2}{18\mu}\boldsymbol{g} \tag{5}$$

where ρ_p and ρ_f are the density of the solid particle and the carrying fluid, respectively, d_p is the representative diameter of the proppant, and μ is fluid dynamic viscosity.

Also, a widely used form of the correction factor is provided by the Richardson & Zaki correlation (1954):

$$f(c) = (1-c)^{4.65} \tag{6}$$

After substitution of Eq.(6) in (4), and of the resulting expression in (3), we obtain:

$$\boldsymbol{v}_p = \boldsymbol{v} + f^*(c)\boldsymbol{v}_{Stokes} \tag{7}$$

where

$$f^*(c) = (1-c)^{5.65} \tag{8}$$

The settling rate coefficient $(1-c)^{5.65}$ is plotted versus volumetric concentration, c in Figure 1. Settling is slower at higher concentrations.

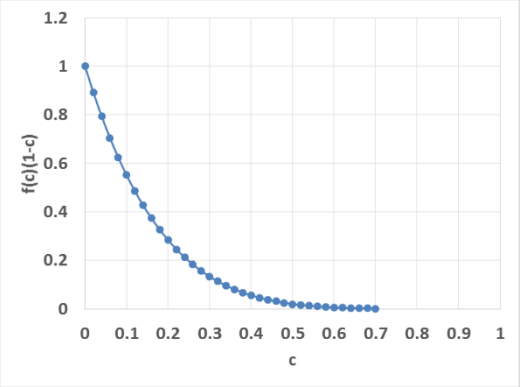

Figure 1. Settling rate coefficient $f(c)$ (1-c) versus concentration, c.

2.2 *Proppant convection*

Another coupling variable of interest is the slurry density, which affects the Reynold's governing equation for the fluid flow. In the proppant logic formulation, the Boussinesq approximation, that fluid density variations due to concentration changes are significant only in their generation of buoyancy forces, is invoked.

In the existing *3DEC* fluid flow logic, the flow rate per unit width of the joint is:

$$\mathbf{q} = -ka\nabla\left(p - \rho\mathbf{g}.\mathbf{x}\right) \tag{9}$$

where $k = a^2 / (12\mu)$ is the joint mobility coefficient, ρ is the fluid (slurry) density, and g is gravity. In the Boussinesq approximation, it is assumed that the fluid density in Eq.(9) relates to the proppant concentration, c by the linear equation:

$$\rho = \rho_f \left[1 + c\left(\frac{\rho_p}{\rho_f} - 1\right)\right] \tag{10}$$

where ρ_f is the density of the carrying fluid, and ρ_p is the density of the proppant.

The effect of the suspended particles on the slurry viscosity is accounted for by adjusting the carrying fluid viscosity as a function the proppant concentration by means of empirical formulae. This coupling functionality is not accounted for directly in the formulation; however it can currently be introduced via *FISH*.

3 NUMERICAL IMPLEMENTATION

The advection equation is solved numerically using a node-centered finite volume approach (for a cell-centered formulation, see LeVeque 2002). The scheme takes advantage of the triangular discretization of the flow planes used in the fluid flow calculations. Also, the nodes are discretization features located at the triangle apex. A control domain is assigned to each node, and the proppant volume fraction, c, the proppant height in the joint, h, together with the joint aperture, a are averaged over the control domain. The boundary of the two dimensional control domain for a particular node is a polygon of straight line segments; two segments are defined per triangle having the node in common, and each segment links the center of the triangle to the mid-point of a side that radiates from the node, see Figure 2.

The proppant volume fraction at a node (located in a joint) is:

$$c = \frac{h}{a} \tag{11}$$

and the proppant height at a node is:

$$h = ca \tag{12}$$

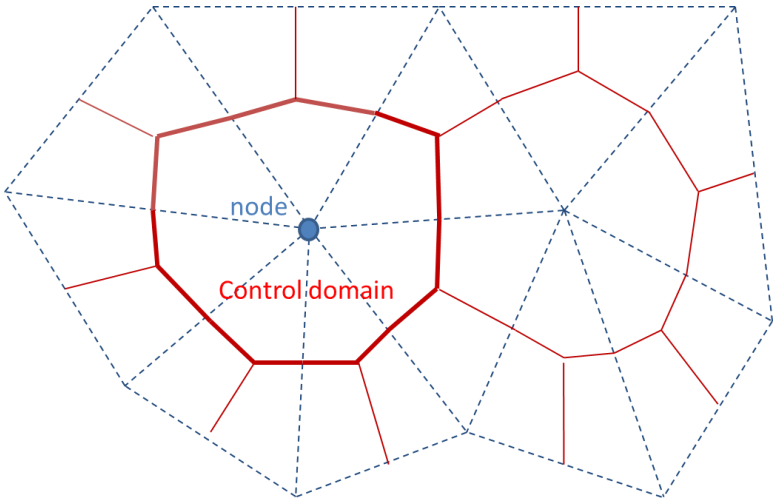

Figure 2. *3DEC* flow plane discretization in triangles (blue) showing node and control domain (red).

To discretize Eq.(1) using the finite volume method, we first integrate over the control domain of area, A:

$$\int_A \frac{\partial(ca)}{\partial t} dA + \int_A \nabla \cdot \left(ca\mathbf{v}_p \right) dA = 0 \tag{13}$$

and then make appropriate approximation for fluxes across the boundary of each control domain.

3.1 *Transport with no aperture change*

We examine each term in Eq.(13), separately for the case when transport is taking place and aperture is not changing.

3.1.1 *Transient term*

When transport is taking place (and aperture is kept constant), the discretization of the transient term integral is given by:

$$\int_A \frac{\partial(ca)}{\partial t} dA = \frac{h^{new} - h^{old}}{\Delta t} A \tag{14}$$

where Δt is the time step.

3.1.2 *Advection term*

The advection term is expressed in terms of the slurry and settling velocities using Eq.(3):

$$\int_A \nabla \cdot \left(ca\mathbf{v}_p \right) dA = \int_A \nabla \cdot \left(ca\mathbf{v} \right) dA + \int_A \nabla \cdot \left(caf^*(c)\mathbf{v}_{Stokes} \right) dA \tag{15}$$

We use Gauss divergence theorem to transform the integral over the control domain into an integral over its polygonal boundary, $\mathcal{C}$:

$$\int_A \nabla \cdot \left(ca\mathbf{v}_p \right) dA = \int_{\mathcal{C}} ca\mathbf{v} \cdot \mathbf{n}\, ds + \int_{\mathcal{C}} caf^*(c)\mathbf{v}_{Stokes} \cdot \mathbf{n}\, ds \tag{16}$$

where $\mathbf{n}$ is the normal to the boundary pointing out of the control domain.

The slurry advection term in Eq.(16) is expressed in terms of flow rate per unit width of the joint, using Eq.(2):

$$\int_{\mathcal{C}} ca\mathbf{v} \cdot \mathbf{n}\, ds = \int_{\mathcal{C}} c\mathbf{q} \cdot \mathbf{n}\, ds \tag{17}$$

The discretization of the slurry advection term is given by:

$$\int_{\mathcal{C}} c\boldsymbol{q}\cdot\boldsymbol{n}\,ds = \sum_s c_s\left(\boldsymbol{q}\cdot\boldsymbol{n}\right)_s L_s \tag{18}$$

where the summation over the boundary segments of a control domain is denoted by $\sum_s$ and L_s is the length of each segment.

The vector $\boldsymbol{n}$ is the normal to the segment pointing out of the control domain centered on point P_1 into an adjacent control domain centered on point P_2, see Figure 3. The value of c_s is determined by the convection scheme adopted to achieve physically realistic solutions. Here, we use an upwind scheme, whereby the advected quantity, c_s is taken upstream from the flow:

$$c_s = \begin{cases} c_{P_1} \text{ if } \boldsymbol{q}.\boldsymbol{n} > 0 \\ c_{P_2} \text{ if } \boldsymbol{q}.\boldsymbol{n} < 0 \end{cases} \tag{19}$$

The upwind scheme is unconditionally stable, however, the solution over predicts the diffusive terms producing numerical smearing of the front. The quality of the solution can potentially be improved using second-order correction terms with flux limiters; however this technique is not implemented in the current version of the scheme.

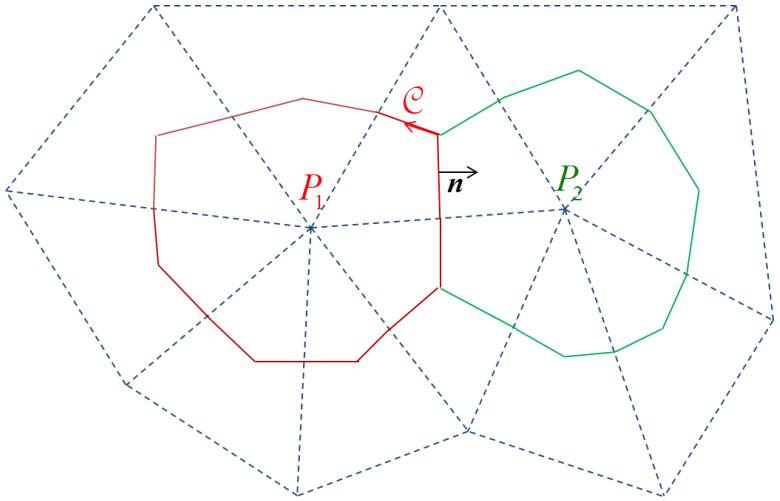

Figure 3. Control domains and quantities used to illustrate the upwind advection scheme.

The settling advection term in Eq.(16) is a non-linear function of the primary variable, c. The discrete form used in the numerical scheme is given by

$$\int_{\mathcal{C}} caf^*(c)\boldsymbol{v}_{Stokes}\cdot\boldsymbol{n}\,ds = \sum_s h_s\left(f^*(\bar{c})\boldsymbol{v}_{Stokes}\cdot\boldsymbol{n}\right)_s L_s \tag{20}$$

where, $h = ca$ (see Eq.(12)), the value of $\bar{c}$ (used to express the correction term f^*) is the average value of c at the three nodes of the triangle containing the boundary segment, and

$$h_s = \begin{cases} \mathrm{h}_{P_1} \text{ if } \boldsymbol{v}_{Stokes}.\boldsymbol{n} > 0 \\ \mathrm{h}_{P_2} \text{ if } \boldsymbol{v}_{Stokes}.\boldsymbol{n} < 0 \end{cases} \tag{21}$$

Combining Eq.(14), Eq.(18) and Eq.(20), the discretization of Eq.(13) is written for each control domain as

$$h^{new} = h^{old} - \frac{\Delta t}{A}\left[\sum_s c_s \left(\boldsymbol{q}\cdot\boldsymbol{n}\right)_s L_s + \sum_s h_s \left(f^*(\bar{c})\boldsymbol{v}_{Stokes}\cdot\boldsymbol{n}\right)_s L_s\right] \tag{22}$$

In the (explicit) time stepping numerical scheme, all the quantities in the right hand side of Eq.(22) are assumed to be known from the previous time step. A new proppant height for the step is evaluated for each node, and the volume fraction is then updated using Eq.(11).

The fluid flow scheme already in place assumes fluid volume balance. Also, the advection scheme conserves proppant volume (there is no lost proppant because it is simply moved from control volume to another in the flow domain); this will be demonstrated in the example below.

3.2 *Mechanical coupling*

3.2.1 *Aperture change with no transport*

In addition to the change in concentration due to advection, the concentration at a node changes with changes in aperture. When no transport is taking place ($\boldsymbol{v}_p = 0$), and the advection equation Eq.(13) simplifies to:

$$\int_A \frac{\partial\left(ca\right)}{\partial t} dA = 0 \tag{23}$$

The equation implies that the product *ca* remains constant. In other words, because the mass of proppant is constant during the mechanical step in which aperture is changed, the new concentration c_1, may be calculated directly from the change in joint aperture (from a_0 to a_1) during the step, as follows:

$$c_1 = c_0 \frac{a_0}{a_1} \tag{24}$$

where c_0 is the concentration before the step.

3.2.2 *Load carried by the proppant pack*

The condition for proppant taking the load is reached when the proppant (volumetric) concentration reaches the saturated value, c_{limit} equal to the ratio between maximum initial (unloaded) density of packed proppant, ρ_0 and the density of the proppant particles, ρ_p.

The general equation for the stress carried by a laterally confined pack of material of maximum initial (unloaded) density, in which an axial displacement, Δu is applied is:

$$\sigma = -\frac{\Delta u}{h_p^*} B \tag{25}$$

where B is the confined modulus (equal to $K + 4G / 3$ for an isotropic material), and h_p^* is the height of the unloaded pack. The relation of fracture-width to stress from tests performed on proppant suggests that the assumption of linearity in Eq.(25) is valid.

Expressing (25) in incremental form, for a fracture of aperture *a*:

$$\Delta\sigma = -\frac{\Delta a}{h_p^*} B \tag{26}$$

This equation is valid only when the condition for the proppant to take the load has been met (i.e. $c > c_{lim}$), and for as long as the total stress, σ remains compressive. If the requirements are not met, the proppant takes no load. The constants c_{lim} and B are input properties for the proppant.

If $\sigma > 0$ in a particular node, the advection of proppant is blocked. However, the carrying fluid is allowed to flow through the pack; the intrinsic permeability of the pack is a user input value.

The mechanical effect of proppant on the normal contact force, F_n, is captured by the following equation:

$$\Delta F_n = -A\left(\Delta P + \Delta\sigma\right) w_f \tag{27}$$

Where $\Delta\sigma$ is the change of proppant stress over one time step, and w_f is an appropriate node-contact weighting factor.

3.3 *Bridging*

The proppant is blocked if the fracture width is small enough, compared to the particle size. The particle size is a user input value.

3.4 *Proppant convection*

The convection mechanism caused by density variation in the slurry is taken into account in the formulation, by adjusting locally the slurry density in the fluid transport equation, according to Eq.(10).

3.5 *Condition at an intersection between flow planes*

The simplified, two plane configuration represented in Figure 4 is used for the discussion.

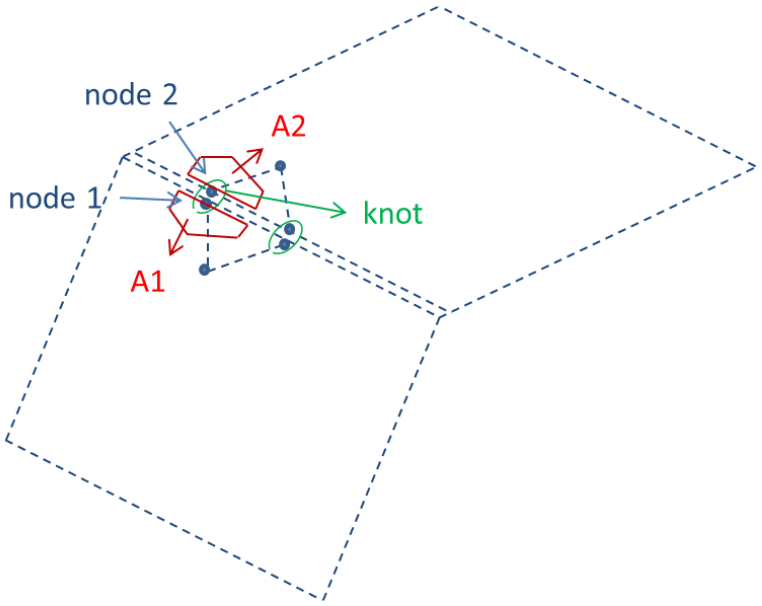

Figure 4. Two intersecting flow planes with discretization triangles, edge nods and control domains (red).

Each flow plane is discretized into triangles; node 1 and node 2, located on the planes intersection, are grouped in a 'knot'. The control domains for node 1 and node 2 are lumped together and the result is assigned to the knot:

$$A_{knot} = A_1 + A_2 \tag{28}$$

Also, the knot aperture is evaluated using an area average at the node quantity:

$$a_{knot} = \frac{a_1 A_1 + a_2 A_2}{A_{knot}} \tag{29}$$

The new proppant height at the knot, h_{knot} is calculated using the numerical scheme described above; the proppant concentration at the knot, c_{knot} is then obtained by dividing proppant height by knot aperture, i.e. $c_{knot} = h_{knot} / a_{knot}$. The knot concentration is assigned to node 1 and node 2,

and the new proppant height at the node is computed by multiplying concentration and node aperture: $h_1 = c_{knot}\, a_1$, $h_2 = c_{knot}\, a_2$. The proppant volume balance at an intersection:

$$h_{knot} A_{knot} = h_1 A_1 + h_2 A_2 \tag{30}$$

is conserved automatically using this scheme.

3.6 *Timestep for stability*

There are two ways to run a fluid-proppant transport calculation: a) uncoupled (the flow calculation is performed first, and the proppant transport next), or b) coupled (the proppant transport calculation is performed after each flow calculation step).

Also, the stable explicit time step for the proppant transport, is in most cases much larger than the explicit fluid flow time step. In uncoupled simulations, the stable time step for proppant transport is calculated by considering the CFL condition (Courant-Friedricks-Lewy) for the discretized form of the one dimensional advection equation:

$$\frac{\partial c}{\partial t} + v \frac{\partial c}{\partial x} = 0 \tag{31}$$

The Courant number is defined in this case, as:

$$\upsilon = \frac{c \Delta t}{\Delta x} \tag{32}$$

where Δt is the proppant time step, and Δx is the discretization length, and the condition for stability is:

$$0 \le \upsilon \le 1 \tag{33}$$

For the *3DEC* uncoupled simulations, we use the following expression of stable time step, based on Eq.(32):

$$\Delta t_p = \alpha \frac{\Delta L_{\min}}{\left| \boldsymbol{v}_{p,\max} \right|} \tag{34}$$

where $\Delta L_{\min}$ is the smallest discretization length, and $|\boldsymbol{v}_{p,\max}|$ is the largest proppant velocity magnitude among triangles in the flow planes.

In coupled simulations, the stable time step is taken to be the same as the explicit fluid step. In coupled fluid-proppant-mechanical calculations, in each calculation step: the fluid flow is carried out first, then the proppant transport is done, finally enough mechanical steps are taken (consistent with the settings) to keep the system in quasi-static equilibrium.

3.7 *Boundary and initial conditions*

Two types of boundary conditions are considered for the proppant transport problem: imposed volumetric flux of proppant, and imposed volumetric fraction.

The second type is difficult to realize physically: it is introduced only to facilitate potential comparison of the numerical results with existing analytic solutions. The proppant volume fraction can be initialized within a geometrical range in the flow planes.

4 VERIFICATION TEST

A simple advection test is conducted to check the functionality of the proppant transport logic in a planar horizontal joint of constant and uniform aperture *a*. The joint is 10 m long, 1 m wide, and aperture is 0.1 mm. A uniform pressure gradient of 0.1 MPa/m is applied in the long direction of the joint. The fluid viscosity μ is 10^{-3} Pa.m. The joint discretization length is 0.25 m. With the parameter values selected for the test, the fluid velocity in the fracture $v = (a^2 / 12 \cdot \mu)\, \nabla p$ is about

8.33 10^{-2}m/s, or 1/12 m/s. The concentration is fixed at 0.3 at the left (short) edge of the joint. The pore pressure contours and velocity vectors in the joint are shown in Figure 5. The profiles of concentration at 12s, 36s, and 60s are plotted in Figure 6.

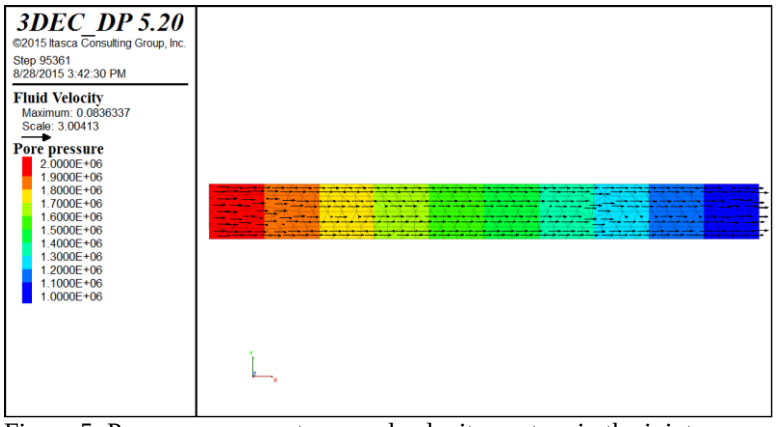

Figure 5. Pore pressure contours and velocity vectors in the joint.

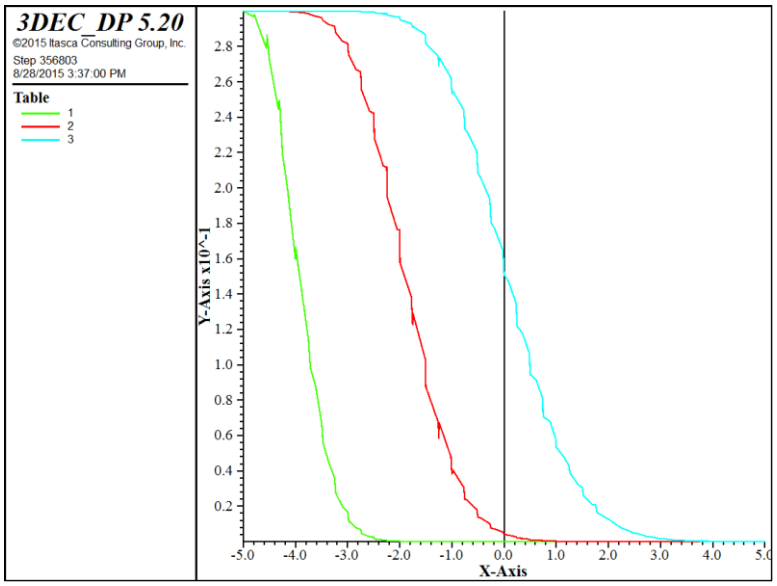

Figure 6. Concentration profile (concentration versus distance).

The pulse front is centered at the expected locations: 1 m, 3 m, and 5 m from the fixed concentration joint edge, but there is some dispersion (spreading of the initially vertical pulse front). Numerical dispersion is common in solving hyperbolic equations like Eq.(1) using conventional upwind techniques. As mentioned in Section 3.1.2, numerical techniques exist to reduce the front dispersion (e.g. by application of a second-order correction with a limiter), but they have not been implemented in this development. Contours of proppant concentration at the corresponding times are shown in Figure 7.

As expected in numerical simulations: the accuracy of the solution can be increased by decreasing the discretization length.

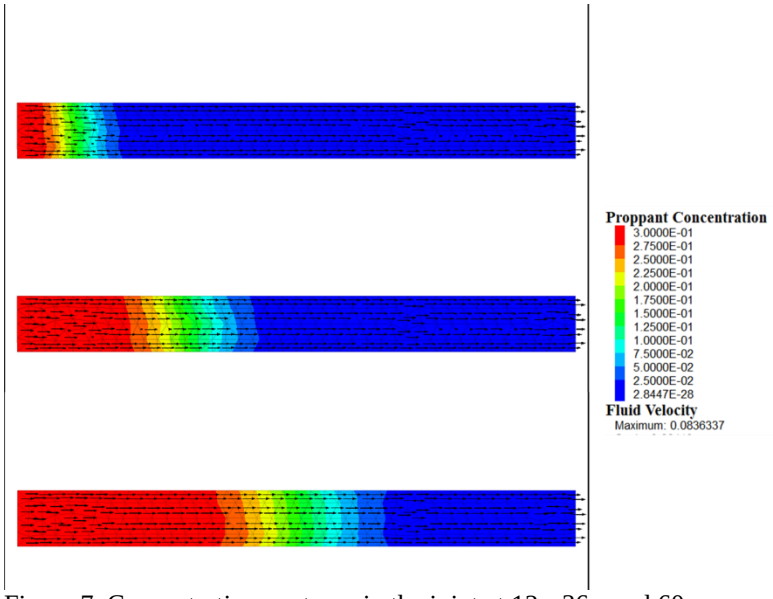

Figure 7. Concentration contours in the joint at 12s, 36s, and 60s.

5 EXAMPLE

Fluid injection in a 10 m × 10 m × 10 m block of elastic material containing two perpendicular fracture planes is simulated in this example. The origin of the coordinate system is at the center of the block. The initial stress in the block is 3 MPa in the x- and z-direction, and zero in the y-direction. The bottom of the block is fixed, and a pressure of 3 MPa is applied at the top. A roller boundary condition is applied at x = -5 m, and a pressure of 3 MPa is applied at x = 5 m. The boundaries of the block in the y-direction are stress free. The first fracture plane is horizontal and goes through the origin of axes; the second fracture is located at x = 2.5 m. The bulk modulus of the elastic material is 5 GPa, and the shear modulus is 2 GPa. The normal stiffness of the fracture is 50 GPa/m, and the shear stiffness is 10 GPa/m. The fracture aperture under zero stress is 0.1 mm, the residual aperture is 0.01 mm, and the maximum aperture is 0.2 mm. A volumetric source of fluid loaded with proppant is applied at x = 0.14 m. The injection rate is 0.01 m^3/s. The carrying fluid has a density of 1000 kg/m^3, a viscosity of 10^{-3} Pa.m, and a bulk modulus of 0.05 GPa. The volumetric concentration of proppant in the injected fluid is 0.1.

The pore pressure contours and specific discharge vectors in the fractures are shown at the end of the 2s simulation in Figure 8 (note that the y-axis is quasi-vertical in the figure).

The fluid has migrated extensively in the first fracture, and has also intruded in the second fracture. The fracture aperture at 2s is plotted in Figure 9. Contours of proppant concentration at the end of the 2s simulation are shown in Figure 10.

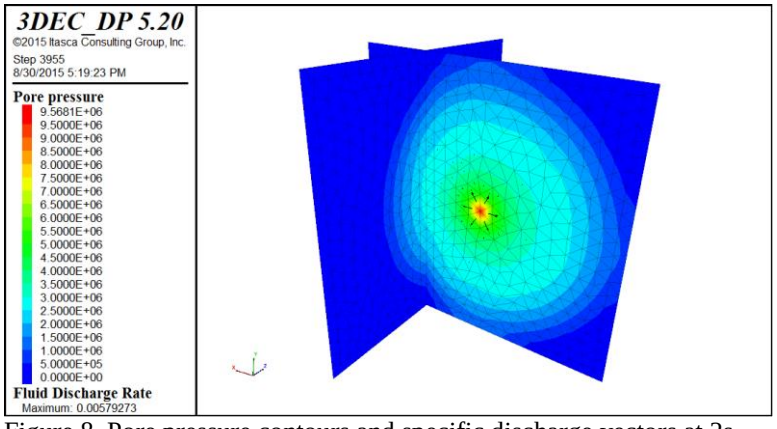

Figure 8. Pore pressure contours and specific discharge vectors at 2s.

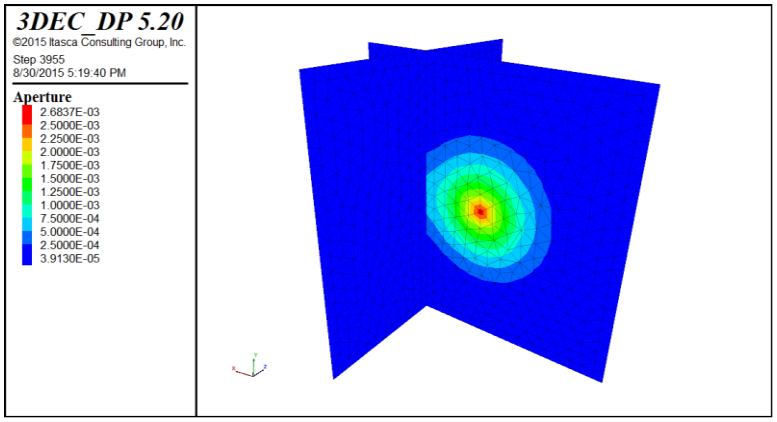

Figure 9. Contours of fracture aperture at 2s.

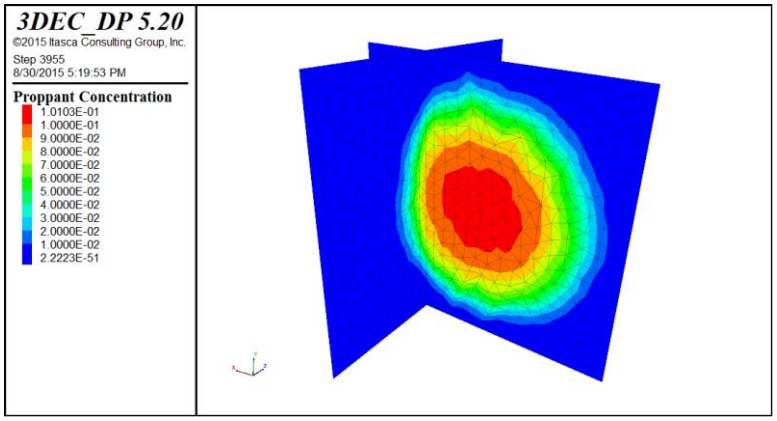

Figure 10. Concentration contours at 2s.

The simulation shows that the proppant has migrated in a radial pattern in the first fracture, and that it has also intruded in the second fracture. Comparison of the proppant volume injected at the source to the volume of proppant distributed in the model (using a *FISH* function) shows that volume balance is satisfied to within a relative error less than 0.2% at the end of the simulation.

6 APPLICATION

A field scale fracturing job is modeled to demonstrate more realistic proppant transport behavior. The rock mass represented in the model is located at a depth of 2250 m to 2750 m, and a 2 MPa step change in stress occurs at 2540 m (60 m above the injection point), as shown in Figure 11.

The rock mass is assumed to be homogenous with constant bulk and shear moduli of 5 GPa and 2 GPa, respectively. A Newtonian fluid with a viscosity of 0.1 Pa·s is injected at 0.05 m^3/s for one hour, and the proppant concentration ramps up gradually from zero in the first 10 minutes to a volume fraction of 0.15 at 50 min, as shown in Figure 12. The proppant size is 0.425 mm (40 mesh). Leakoff of fluid into the matrix is ignored because the rock is assumed to have a very low permeability.

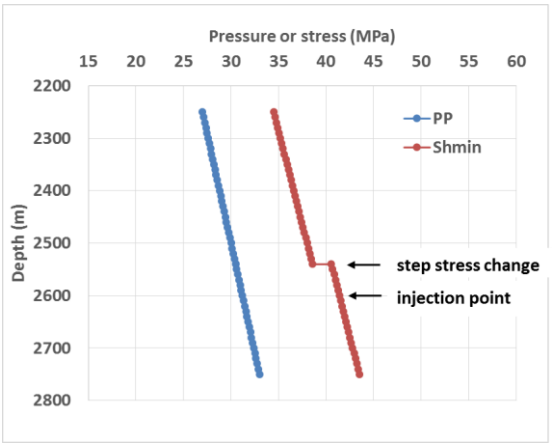

Figure 11. Pore pressure and minimum horizontal stress along the depth.

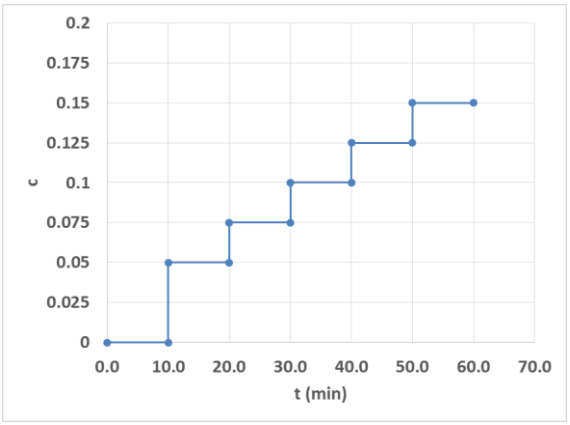

Figure 12. Proppant pump schedule with ramp up of proppant concentration.

Figure 13 shows the fracture aperture at 30 min and 60 min. The fracture initially propagates as a radial crack from the injection point. The full hydro-mechanical coupling results in pinching and a low aperture at the interface between the stress layers. Mechanically the fracture has a tendency to propagate upward rapidly once it reaches the step change in stress (due to the lower stress), which would require a large volume of fluid to fill the rapidly opening fracture. However, the pressure drop on the bottom layer increases due to the increasing flow speed which results in the tighter compression of the stress to form the pinch. The height growth is controlled by the pressure drop and flowrate across the interface.

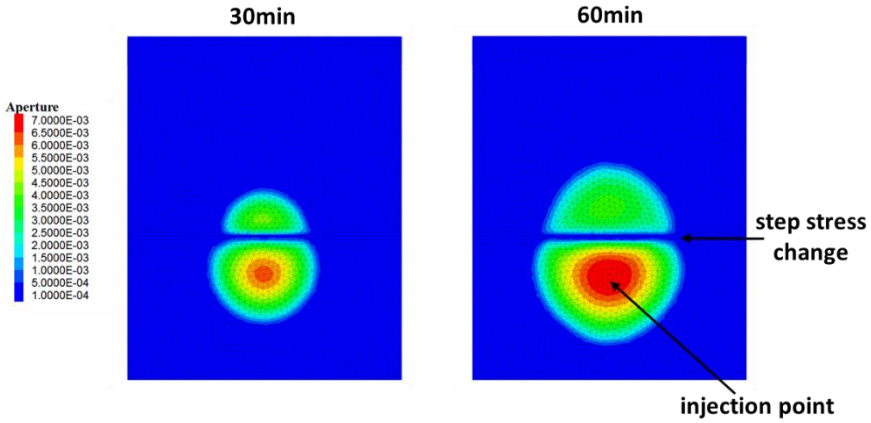

Figure 13. Contour of fracture aperture at 30 min and 60 min injection.

Figure 14 shows the proppant concentration at 30 min and 60 min. By 30 min, an area of high concentration area has formed along the pinch line and no proppant has entered the top layer, indicating that proppant is "bridged" along the interface of step change in stress. By 60 min, the area of proppant distribution has expanded in the bottom layer, but still no proppant can pass through the pinch line. The proppant concentration in some sparse areas along the interface has reached the "pack" limit of 0.7. Once "bridging" or a "pack" has formed, it is treated as a permeable medium through which fluid can flow. In this case, the pack permeability is set to be 0.01 times the permeability of an open channel of the same width (no proppant). This results in a significant decrease of fluid supply into the upper layer.

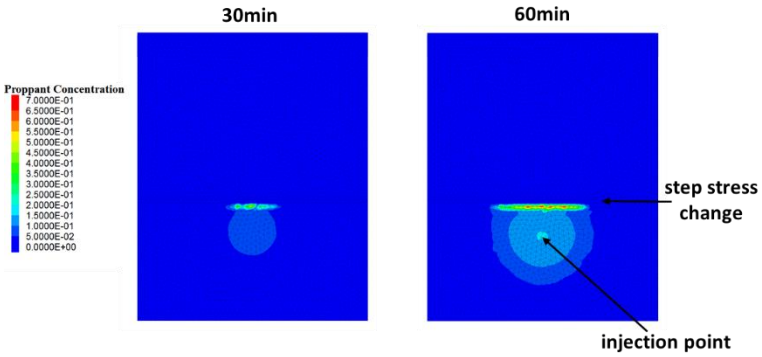

Figure 14. Proppant concentration contour at 30 min and 60 min.

7 CONCLUSIONS

A scheme to model proppant transport in fractures has been designed and implemented in the *3DEC* code. The logic takes into account fluid-mechanical coupling and several effects are represented, such as pack-formation, bridging, proppant convection, and settling. The theoretical basis and the numerical implementation of the scheme have been described in the paper. A simple verification test, and example simulation have been presented to illustrate some of the features.

ACKNOWLEDGEMENT

The support and contribution of Jim Hazzard to this development is deeply appreciated. Also, thanks are extended to Mark Mack and Shawn Maxwell, without whom this work could not have seen the light of day.

REFERENCES

Adachi, J., Siebrits, E., Peirce, A. & Desroches, J. 2007. Computer simulation of hydraulic fractures. *Int. J. Rock Mech. & Mining Sci.* 44**:** 739-757.

Courant, R, Friedrichs, K & Lewy, H. 1928. On the partial difference equations of mathematical physics. *Mathematische Annalen*, 100, 32–74. English translation in IBM J. (March, 1967) 215–234.

Itasca Consulting Group, Inc. 2013. *3DEC – Three Dimensional Discrete Element Code, Version 5.0*. Minneapolis: Itasca.

LeVeque, R.J. 2002. *Finite Volume Methods for Hyperbolic Problems*. Cambridge University Press, London.

Richardson, J.F. & Zaki, W.N. 1954. Sedimentation and Fluidisation. Part I. *Trans. Inst. Chem. Engrs* 32, 35-53.